High-resolution diffusion MRI studies of development in pregnant mice visualized by novel spatiotemporal encoding schemes

(article begins on next page)

High definition diffusion MRI: Principles and applications to visualizing pregnant mice development

Qingjia Bao, Gilad Liberman, Eddy Solomon and Lucio Frydman*

Department of Chemical and Biological Physics, Weizmann Institute, Rehovot 76100, Israel

Keywords: diffusion-weighted imaging, spatiotemporal encoding, pregnant rodents, fetal development, placental maturation

Abbreviations: ADC, Apparent Diffusion Coefficient; EPI, Echo Planar Imaging; DWI, diffusion weighted imaging; FOV, Field of View; FSE, Fast Spin Echo; FT, Fourier transformation; PE, phase encoding; SPEN, spatiotemporal encoding

Running Title: *Visualizing pregnant mice development by in vivo diffusion MRI*

Word count: 2,995 in main text (including Methods)

Figures: 8 in the main text, 8 in the supporting extended data

Tables: 0

Equations: 0 in main text, 1 in supporting information and extended data

References: 51 in main text, 7 in supporting information and extended data

*Prof. Lucio Frydman; +972-8-9344903; lucio.frydman@weizmann.ac.il

Summary

This study introduces an MRI approach to map diffusion of water *in vivo* with high resolution under challenging conditions; the approach's potential is used in diffusivity characterizations of embryos and fetoplacental units in pregnant mice, as well as of newborn mice in their initial postnatal period. The method relies on performing self-referenced spatiotemporal encoded MRI acquisitions, that can achieve the motional and susceptibility immunities needed to target challenging regions like a mouse's abdominal cavity in a single-shot. When suitably combined with zoomed-in and with novel interleaving procedures, these scans can overcome the sensitivity challenges arising upon targeting $\approx$100μm resolutions, and target longitudinal development in abdominal organs that have hitherto eluded *in vivo* diffusion-weighted imaging (DWI). This is here employed to follow processes related to embryonic implantation and placentation; including mouse gastrulation, the development of white matter in fetal brains, the maturation of fetal spines, and the evolution of the different layers making up mice's hemochorial placentas. The protocol's ability to extract robust diffusion maps in challenging regions as a function of embryonic mice development is thus demonstrated, and its usefulness as tool for visualizing pregnancy-related developmental changes in rodents is discussed.

Introduction

Nuclear Magnetic Resonance Imaging (MRI) is a mainstream approach to unravel *in vivo* morphology and physiology, both in preclinical (animal) and human studies. One of MRI's main applications concerns its use to measure water's apparent diffusion coefficient (ADC) in living tissues via diffusion-weighted imaging, DWI[1–3]. Given the connection between these microscopic displacements and tissue morphology, DWI provides an indirect way to highlight structures and architectures that are often too small for being directly imaged[4–7]. Diffusion MRI also provides insight about perfusion and capillary flow within tissues, and delivers this information with a penetration power unavailable to most other non-invasive imaging methods. DWI provides its rich structural and dynamic information by relying on pairs of pulsed magnetic field gradients possessing equal but opposite actions[8]; by measuring the attenuations that these bipolar modules impart on the NMR signal, it is possible to compute the extent and directionality of the intervening microscopic motions.[1–10] As a result of the spontaneous motions that unavoidably arise in living organisms, multi-scan imaging approaches are usually avoided in *in vivo* determinations of this kind. Instead, DWI tends to rely on single-scan "ultrafast" methods such as echo-planar imaging (EPI[11–13]) in order to retrieve its information. EPI can deliver quality 2D images in a single scan, yet its application is limited to relatively homogeneous organs –the human brain being a prototypical example of this. This is a consequence of EPI's sensitivity to field heterogeneities[14–16], a problem that has triggered the search for variants suitable for targeting other challenging organs and environments[17–24]. Spatiotemporal encoding (SPEN) approaches that overcome field distortions thanks to their reliance on stronger imaging gradients and enhanced T_2^* refocusing abilities,[25,26] have also been explored for these aims. SPEN's robustness has been demonstrated in DWI analyses of challenging regions for both animals[27–29] and humans[30,31], including abdominal studies of small pregnant rodents[27]. Still, even these procedures were constrained by the limited sensitivities they could achieve in a single shot, which defined in turn the maximal resolution of the features that could be imaged. To solve this challenge alternatives have been proposed based on multi-scan interleaving[32,33]. SPEN is also a practical starting point for implementing this kind of multi-shot scanning, as by contrast to traditional MRI it provides its low-bandwidth (phase-encoded) information directly in the spatial domain. This makes it possible to correct for potential artifacts in a self-referenced, scan-by-scan manner[34,35]. The present study exploits this feature, together with a new interleaving procedure

and a customized image rendering protocol, to develop a tool for mapping at high resolution abdominal mice regions. This is illustrated by the results in Figure 1, which compares *in vivo* features observed in anatomical image collected on the abdomen of a pregnant mouse, against SPEN-based counterparts. Also shown in the lower panels are the apparent diffusivity coefficient (ADC) maps associated to these SPEN acquisitions, defining the mobility of water in the abdominal region. A number of clear anatomical features are shared by all the images, including individual sacs containing the fast-diffusing amniotic fluid, a delineation of fetal brains and spines with distinctly slow ADC values, placental layers including a maternal-side and a fetal-side layer separated by a slower-diffusing interphase, fast diffusing features associated to the umbilical cord, and dark fetal regions delineating the positions of the (slowly-diffusing) liver and (rapidly-diffusing) heart. The present study summarizes the provisions taken for implementing this kind of diffusion measurements, and explores their potential to follow the development of pregnancy in live mice –from a pre-implantation period and throughout the fetal and placental maturation processes. Insight obtained regarding the development of newborn rodents in the few first days post-partum is also presented.

Methods

High definition SPEN DWI. In order to enable the spatial resolution needed to target diffusional features in live fetuses (Fig. 1), a number of changes had to be introduced on the original SPEN acquisition protocols we have used on animals and humans[27,31]. A detailed description of these acquisition and processing changes is deferred to the Supporting Information; yet their main features can be appreciated from the sequence and scanning trajectories introduced in Figure 2. As shown in these schemes experiments were based on multi-shot interleaved procedures – interleaving being necessary for overcoming the sensitivity penalties associated to both high spatial resolution and the losses imposed by the diffusion-weighting gradients. The experiments also exploited the built-in "zooming" qualities that adiabatic sweeps endow on SPEN, for targeting the fetoplacental units without suffering from foldover artifacts arising from elsewhere in the dam. The acquisition scheme also differed from past interleaving alternatives[34,35] by the addition of a delay between interleaved data sets to account for the discontinuities otherwise arising along the SPEN dimension from ΔB_o inhomogeneities and T_2 decays, and by an

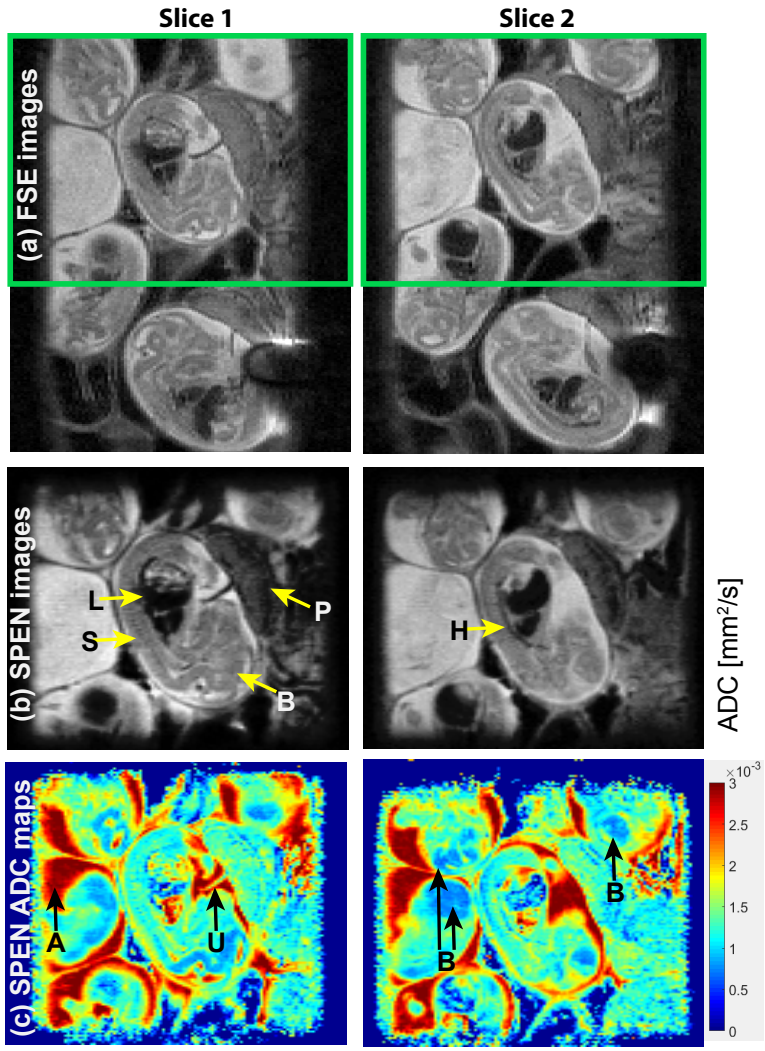

Figure 1. Coronal slices acquired on a pregnant mouse at E14.5. (a) High-definition anatomical (fast spin echo, FSE –also known as RARE) images collected with a 180 μm in-plane resolution (TR/TE = 2000/48 ms, slice thickness=1mm, echo train length = 8, two averages, scan time around 90 seconds with respiratory trigger). (b) SPEN b0 images focusing on the green regions, collected at 119 μm in-plane resolution using the SPEN DWI protocol introduced in this work (Fig. 2 with TR/TE = 2000/40 ms, thickness=1mm, five alternative interleaved shots, four averages, scan time around 60 seconds with respiratory trigger). (c) Apparent Diffusivity Coefficient maps (ADC, in mm^2/s) associated to the SPEN acquisitions (δ=3.6ms, Δ=7.5ms, diffusion gradient strength= 30 Gauss/cm, three orthogonal directions diffusion weighting. Highlights include a multi-layered placenta (P), fetal brains (B), liver (L), spine (S) and heart (H), an umbilical cord (U) and fast-diffusing amniotic fluid (A).

alternation in the k_{RO} readout direction among the interleaved scans that served to uniformly spread the density of points arising from $+G_{RO}$ and $-G_{RO}$ subsets (Fig. 2b). This provided an improved support for mapping, unwrapping and thus compatibilizing the phases arising the all-even ($+G_{RO}$) and all-odd ($-G_{RO}$) data sets, without requiring the use of navigator scans. Compensation for the phase distortions arising between these all-even and all-odd row acquisitions and between the multiple shots, was also customized with a two-stage correction process: first (Figure S1, left-hand column) a coarse overall correction was done on the two super-resolved SPEN images arising from these individual sets; after accounting for these even/odd effects (which are usually dominant in small-bore scanners), a second phase correction loop was applied (Fig. S1, right-hand column) to remove motion-derived inter-shot

imperfections. For both of these phase-correction procedures a new 2D referenceless phase correction method was also devised (Fig. S2), operating in both image and *k*-spaces. Supporting Figures S3 and S4 further explore the efficiency of these new 2D phase correction methods using both synthetic and experimental data. The sequences and data processing protocols required to execute these experiments on either Agilent (VNMRJ 3.2) or Bruker (PV 6.0) scanners, can be downloaded from http://www.weizmann.ac.il/chemphys/Frydman_group/software.

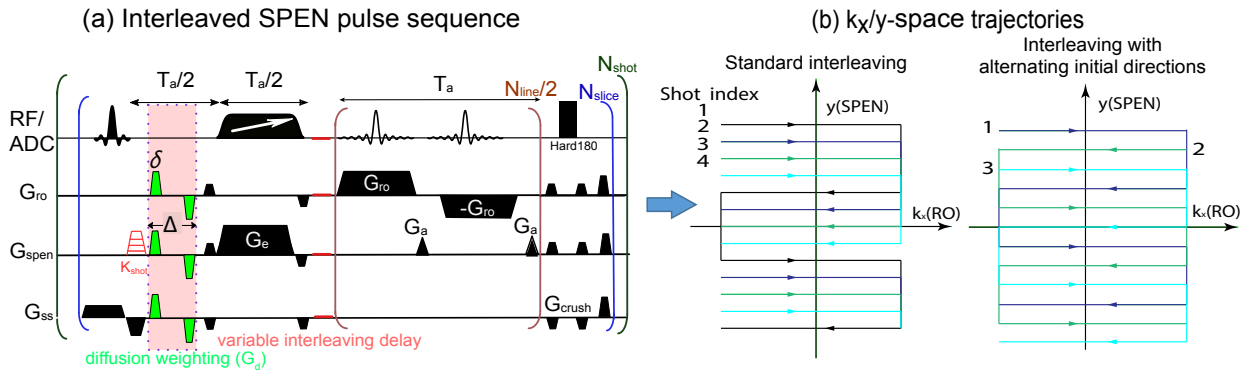

Figure 2. (a) Interleaved SPEN pulse sequence including a diffusion weighted block and gradient (G_d, in green); an RF/ADC line displaying the pulses and signal detection; G_{ro}, G_{spen} and G_{ss} lines displaying the gradients along readout, SPEN (phase-encoding) and slice-selection directions; N_{line}, N_{slice} and N_{shot} denoting the number of SPEN-encoded lines per-shot, the number of slices and the number of interleaved shots respectively; and a $K_{shot} = l \cdot \Delta k$ gradient pulse with corresponding delay $(l-1) \cdot T_a/N_{shot}$ (in red) to perform multi-scan interleaving while keep phase-encoding, amplitude and phase continuity. The SPEN encoding includes a slice selection, a delay $T_a/2$ to achieve full refocusing, encoding via a WURST-shaped adiabatic 180° sweep, and a hard 180° pulse to enable multi-slice operation without saturation. (b) Different k_x/y scanning trajectories associated with standard SPEN interleaving and with the new interleaving procedure proposed in this work. Notice how data interleaving using this alternating acquisition mode, provides a uniform grid of equally-spaced points along the SPEN axis from all-even or all-odd acquisition lines.

MRI scans. Animal experiments were preapproved by the Weizmann Institute IACUC system, which is fully accredited by the AAALAC, the US NIH Office of Laboratory Animal Welfare, and the Israel Ministry of Health. Healthy ICR mice, naïve (n=3) and pregnant (n=8), were studied. The pregnant mice were scanned at stages ranging from E6.5 to E19.5, with pregnancies timed at E0.5 on the morning following overnight pairing of males and females after attesting for the mating. Following the fetal deliveries, *in vivo* experiments on *n*=5 neonatal mice were also continued for three days post partum. All data were collected on a DD2® 7T/110mm horizontal magnet scanner (Agilent Technologies, Santa Clara, CA) equipped with a 100 G/cm maximum gradient triple-axis setup, using a quadrature 40 mm volume (Millipede®) coil; respiratory

triggering was used for all the adult mice experiments but not for the neonatal scans, as respiratory signals were in these cases too weak. Adult mice were anesthetized with isoflurane (1-2%) via a vaporizer, and the animals' body temperatures were maintained constant by using a water-based heating system. Respiration was monitored via a pressure sensor (SA-II, Stony Brook, NY) and maintained at 30–50 breaths per minute. For these abdominal scans animals were not fixed. The neonatal mice were anesthetized using a 0.5% O_2/isoflurane mixture and strapped to a foam bed during their scans; these were limited to less than 40 min total and animal well-being was followed with a pressure-based respiratory sensor. In the bulk of these scans the SPEN sequence shown in Figure 2 was used, and compared against a series of EPI counterparts that included scanner-provided sequences including correcting navigators, as well as custom-written reversed-phase-gradient approaches[36–39]. For anatomical references, scanner-provided fast spin-echo (FSE) sequences were also used, with scanning parameters as included in the caption to each figure. DWI maps were set up by relying on nominal diffusion-weighting values, but processed after computing full effective b-maps incorporating both these pulsed gradient values as well as their cross-talk with the imaging gradients[40].

Results

Figure 3 illustrates the ability of the new SPEN protocol to quantitatively map diffusion at high resolution, by comparing its outcome against that of a lengthier spin-echo (FSE with RARE factor of 1) diffusion measurement on a phantom-like system. Targeted in this *ex vivo* study was a fetus extracted at E15.5 from a pregnant mouse. Main common organs can be clearly identified in both the SE and SPEN experiments for the various slices, and similar ADC information conveyed by the two sets. An additional, coronal-slice comparison between these sequences for an embryo extracted at E16.5, is presented in Supplementary Figure S5.

Figure 4 compares representative *in vivo* DWI results obtained using the SPEN-based procedure introduced above, against single- and multiple-shot EPI results recorded on the abdomen of the same animal at day E12.5 of pregnancy. These 2D coronal slices, including the b0 images and quantitative ADC maps, were recorded with similarly large bandwidths (625kHz for all readouts, 220/320 μs readout times for single-/multi-shot experiments respectively); the

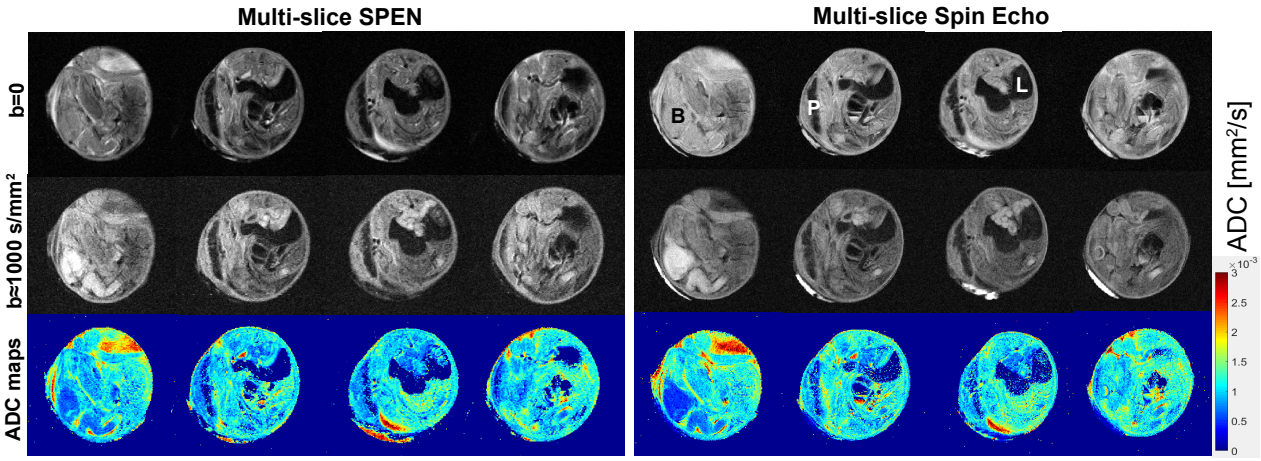

Figure 3. Axial b0, b-weighted and ADC images arising from multi-slice Spin Echo (SE) and SPEN MRI experiments for an *ex vivo* fetoplacental compartment extracted on E15.5 and scanned within the hour. SE parameters: TR/TE=1200/20ms, in-plane resolution=98x98 μm, 1mm slice, two averages, total scan time = 41min; diffusion parameters: δ=3.0ms, Δ=15ms, G_d=30G/cm (corresponding to a b_{max} value=888 s/mm^2). SPEN parameters: TR/TE=1200/40ms, resolution=98x98 μm, 1mm slice, eight averages, total scan time = 8 min; diffusion parameters δ=3.0ms, Δ=12ms, maximum G_d=35G/cm. B: brain; L: liver; P: placenta. The bright, fast-diffusing region probably arises from the embryo's bladder.

spin-echo (SE) EPI experiments incorporated additional reversed-phase-polarity and navigator (reference) scans[37-39] for correcting non-idealities. Although the T2/T2* contrasts of both experiments are slightly different, fetoplacental units are well represented in all b0 images; also similar are the ADC maps arising from these single-shot experiments –even if SPEN shows a slightly increased robustness thanks to its fully-refocused nature and larger effective gradients along the low-bandwidth dimension (≈11.8kHz in SPEN compared to ≈4.5kHz in EPI). Simultaneous resolution and sensitivity improvements over these data are afforded by interleaving, as can be seen from the corresponding b0 images (Fig. 4, right-hand side). Discernable distortions, however, arise in the ADC maps derived from the interleaved SE-EPI data, reflecting the deleterious effects that phase shifts arising from the combination of random tissue movements and the strong diffusion-sensitizing gradients, impose on this approach. By contrast interleaving endows an unambiguous improvement to the SPEN data, with no noticeable artifacts in either the b0 images or the ensuing ADC maps. Similar effects for a second study performed with different b-values on a pregnant animal at day E13.5, are presented and discussed in Extended Data Figure S6.

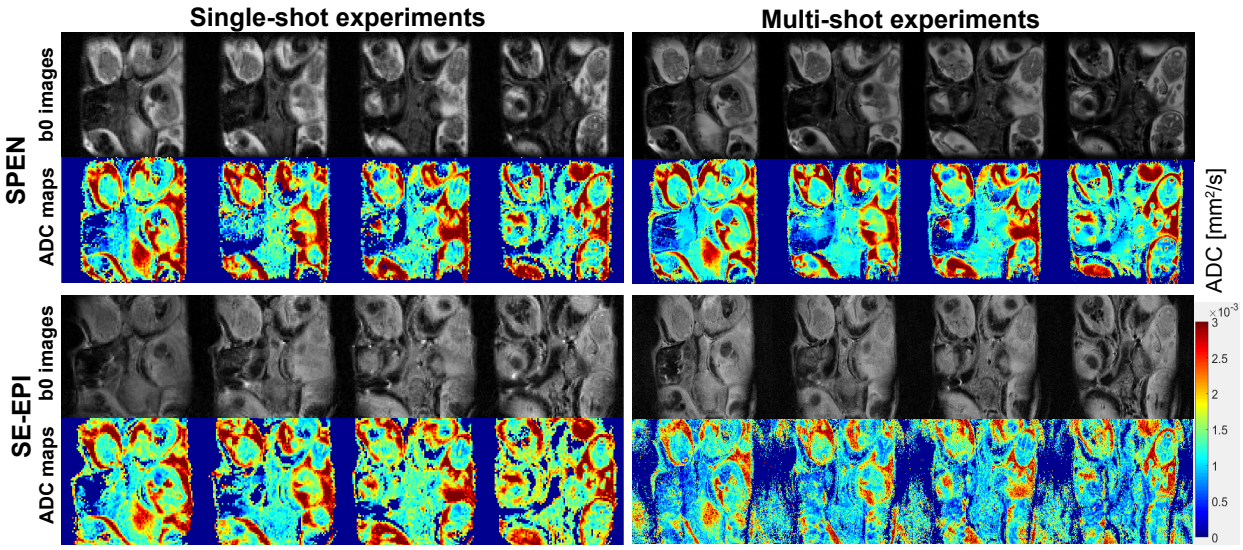

Figure 4. Comparisons between single- and multi-shot (interleaved) SE-EPI and SPEN results obtained *in vivo* on a pregnant mouse at E12.5. Grayscale data show b0 images; colored data are the corresponding ADC maps with the scale given in mm^2/s. Slice thicknesses and read-out bandwidths were in all cases 1 mm and 625kHz; diffusion parameters were δ=3.2ms, Δ=10ms, diffusion gradient = 35G/cm (b-weighting $\approx$ 850 s/mm^2), three orthogonal G_d orientations. Single-shot EPI parameters: TR/TE= 2000/26ms, FOV=30x30mm, data matrix=96x96, extra reference scan for correcting even/odd correction and reversed PE polarity scans to overcome field inhomogeneities[37–39], 2 averages. Single-shot SPEN: TR/TE= 2000/38ms, FOV=32x30mm, data matrix=96x96, no extra scans, 4 averages. Multi-shot EPI: TR/TE = 2000/30 ms, FOV=35x30mm, data matrix=160x160, 5 interleaves, 4 averages. Multi-shot SPEN: TR/TE = 2000/37ms, FOV=32x30mm, data matrix=160x160, 5 interleaves, 8 averages (to keep the same number of scans as in the reversed-phase-polarity EPI scan).

Figure 5 presents SPEN-based DWI analyses on early stages of embryonic development, collected for the same pregnant mouse. The first days precede placentation, and in them multiple embryos developing from ca. 1.5 mm (E6.5) to 3.5 mm (E8.5) in diameter are discernible in the maternal abdomen. The morphologies of these embryos are dominated by a shorter T_2, slower diffusion core (bright ovals in Fig. 5's high-b-value images collected for E6.5 and E7.5), which we ascribe to the extraembryonic ectoderm[41]; for most sacs this slow-diffusion oval contains a faster diffusion feature, likely to be the epiblast. Examination of the ADC maps also shows that these slow-diffusing masses are surrounded by ca. 100μm thick, fast diffusivity layers, probably containing maternal vessels nourishing the embryos prior to the placental formation. Additional grastulation developments are evident at E8.5, with ectoderm, mesoderm and various somites becoming visible in the b≠0 images. At E9.5 the distinct, fast-diffusing signatures of amniotic fluid are observable for several sacs, and so are slow-diffusing features characteristic of the

embryos heads. The fetus and its organs become clearer from E10.5 onwards; from this age on it is also possible to discern well-resolved placental structures possessing distinct ADC layers. Additional illustrations of these developmental features, arising from a different animal and collected under slightly different acquisition conditions, are presented in the Extended Data Figure S7.

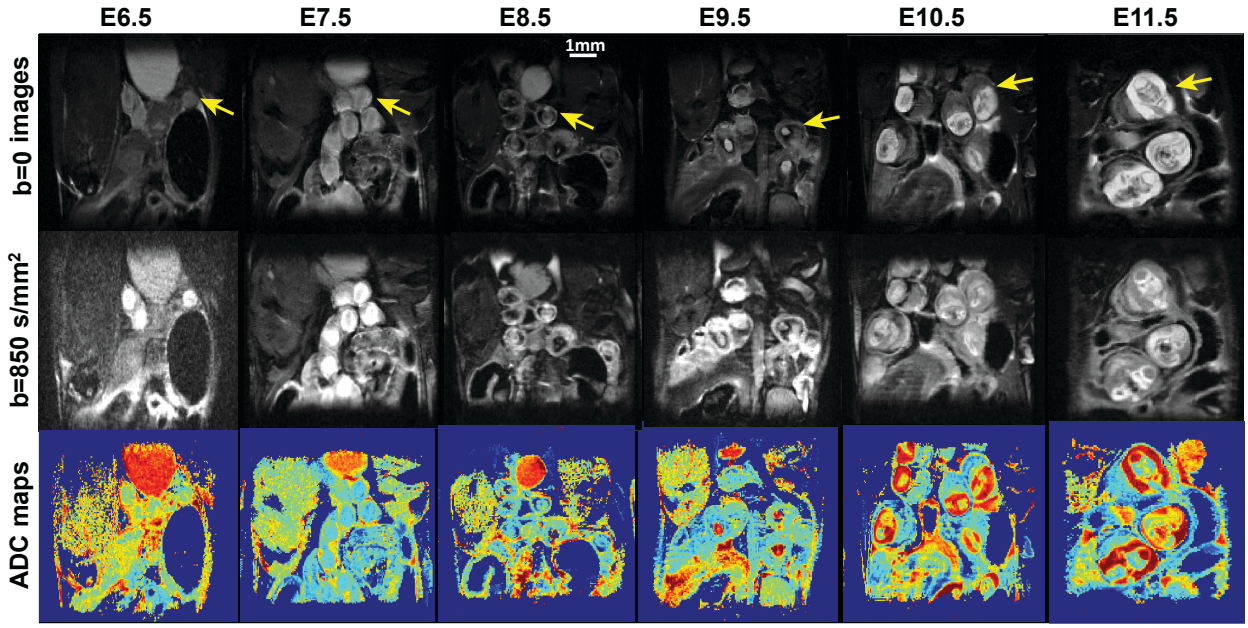

Figure 5. *In vivo* coronal images collected on a pregnant mouse between days E6.5 and E11.5. Shown in grayscale are SPEN b0 and b-weighted images; shown in color are the derived isotropic ADC maps. Indicated by the arrows are some of the embryos, developing into fetoplacental units past day E9.5. All data were collected on 1mm slices on a zoomed 26x26 mm FOV with a 160x160 data matrix (162 μm nominal resolution). Parameters: TR/TE 2000ms/38ms, 5 interleaves, 4 averages, readout bandwidth = 250 kHz. Diffusion parameters: δ=3.2ms, Δ=12ms, diffusion gradient = 30G/cm.

Figure 6 expands this diffusivity analysis with coronal measurements showing finer fetoplacental details, arising at a mode advanced pregnancy stage. These b0 images and their associated ADC maps reveal numerous gestational sacs where the hemispheres in the fetal brains can be discerned, including clear distinctions between CSF and white matter structures; some of these fetal brain characteristics have also been recently reported based on acquisitions combining selective 2D pulse excitations followed by diffusion-weighted GRASE acquisitions[22]. These data also reveals layered structures for both the b0 and ADC maps of most placentas; such layering of the diffusivity characteristics was missed in our earlier, lower-resolution placental ADC studies[27]. Fetal hearts, lungs and umbilical cords, are also discerned in the various slices.

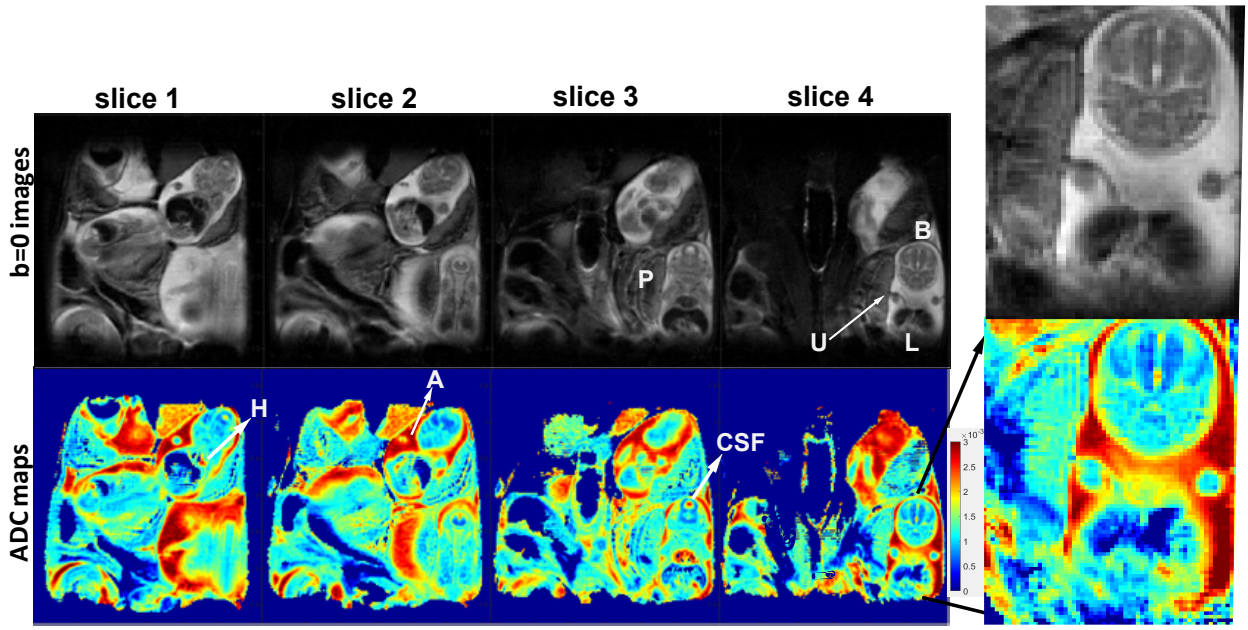

Figure 6. *In vivo* coronal studies of an E18.5 pregnant mouse; shown in grayscale are SPEN-derived b0 images and shown in color are the corresponding ADC maps. Data were collected at a 187 μm in-plane resolution and show, *inter alia*, a fetal heart (H), brain (B) and liver (L), the amniotic fluid (A), placentas (P) and the umbilical cord (U). FOVs and thicknesses for all slices were 30x30x1 mm^3; highlighted on the right-hand side are x4 expansions of the region bound by the black arrows. SPEN parameters: TR/TE 2000/42ms, 5 interleaves, 4 averages, diffusion parameters as in Figure 5.

Figures 7 summarizes additional aspects concerning fetoplacental maturation, based on average ADC values observed upon segmenting different organs as a function of embryonic day for an n=8 cohort of animals –each one containing an average of n=3 fetoplacental units. Figure 7a describes the monotonic decrease in the average ADC value evidenced by fetal brains with age. This is in agreement with what is known from the maturation of human brains[42]. These measurements were also extended to live, neonatal pups; Supplemental Figure S8 illustrates images collected on one such newborn on the third post-partum day. When compared to the trends observed *pre partum* (Figure 7a) it is possible to notice a temporary stop in the monotonic ADC decrease –and presumably in some aspects of the maturation– of the brain around delivery time, followed by a further decrease in the ADCs into values that are common in juvenile brains (which have been reported on the order of 0.72x10^{-3} mm^2/s[43]). A similar plateauing is evidenced for the fetal spines, which although harder to segment than the brains can still be identified and their maturation measured (Fig. 7b).

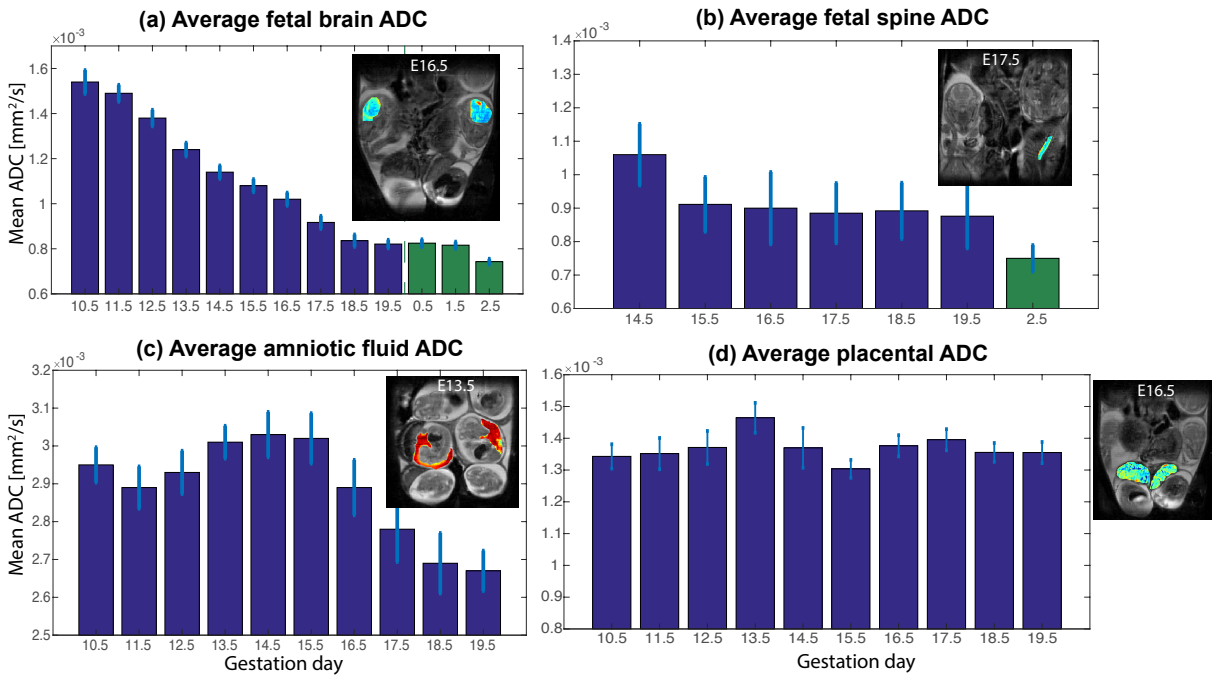

Figure 7 Systematic analyses of the average ADC values measured in fetal brains, spines, placentas and amniotic fluid, in pregnant mice and immediately post-partum. Results show average values arising from 24 fetoplacental units, segmented as illustrated in the various insets here presented. Blue columns correspond to *in vivo* measurements before delivery; green columns to *in vivo* values measured after delivery. Error bars for each measurement represent the spread in average values detected for the mean ADCs over the full cohort. All data were collected under acquisition conditions similar as those described in Figures S7 and S8.

Figure 7c illustrates the progress of the amniotic fluid's ADC with gestation, evidencing a transition from what is in essence a water-like diffusivity ($3x10^{-3}$ mm^2/s at 37 °C) throughout most of the pregnancy, to statistically lower values towards the delivery date. This can be traced to a reduction in the amniotic fluid volume[44,45], something that our data also observes. This in turn has been correlated to an increase in viscosity and in osmolality over the last days of murine pregnancies, which could bring about the observed drop in the ADC of the remaining fluid.

By contrast to the systematic maturation evidenced by CNS organs over pregnancy, placental ADCs show little change when monitored over gestation (Fig. 7d). This is in agreement with two-date measurements previously carried at lower resolution on rats[27], as well as with measurements carried out on human placentas[46]. In fact, the latter show a systematic decrease when including b = 0 values but no systematic trend when measurements are done starting at b ≥ 50 s/mm^2; as SPEN measurements are characterized by intrinsically high (≈50 s/mm^2) b-weightings even in the absence of diffusion-sensitizing gradients, the latter scenario applies also

to the present studies. The overall values observed for the average placental ADCs in Fig. 7d agree, within experimental error, to those reported in a previous lower resolution study. Still, the higher resolution provided by the scan interleaving procedure introduced in this work, allows one to discriminate diffusivity within morphologically distinct placental structures. These in general show three distinct layers (e.g., Figs. 1, 6 and 8), which persist from the initial days of placental formation (E10.5-E11.5) to the final days pre-delivery (E19.5-E20.5). They include a high ADC value region closer to the fetus; a second, larger layer closer to the maternal side characterized by slightly lower ADC values; and a hypointense interphase possessing a shorter T_2 and the slowest ADC values that thinly separates the two regions. On the basis of anatomical observations we ascribe the more distal fetal layer to the maternal decidua, the layer next to the fetus to the maternal/fetal labyrinth, and the trophoblasts to the pearled stratum separating the two. The ability to discern these regions opens the opportunity to characterize diffusivity in the two main layers; Figure 8 illustrates close-ups of the decidual and labyrinthic compartments and compares the evolution of ADCs for these structures with gestation. Although no changes are observed with maturation a statistically significant difference arises between the ADCs of both layers, with the decidual layer showing systematically higher ADC values. This behavior is opposite to that evidenced by perfusion studies based on contrast agents[47], and to the best of our knowledge it has not been seen before.

Discussion and Conclusions

Advancing MRI's capabilities is essential to improve the understanding of biological – and eventually biomedical– features. Diffusion monitoring sequences play a leading role in enabling such investigations, thanks to the unique information that DWI provides about the dynamics of fluids and about the structures that contain them. The need to deal with the confounding effects of motions has made EPI the preferred modality employed in these studies, yet EPI's limitations in dealing with field or tissue heterogeneities limits the kind of organs and situations that are normally tackled. The present study explored a way of extending diffusion studies, so that they can be routinely applied to animal abdominal regions that have hitherto escaped the realm of high definition DWI analyses. Key in enabling such extension was a novel way of sampling the relevant k_x/y-space in order to deal with even/odd imperfections, and phase

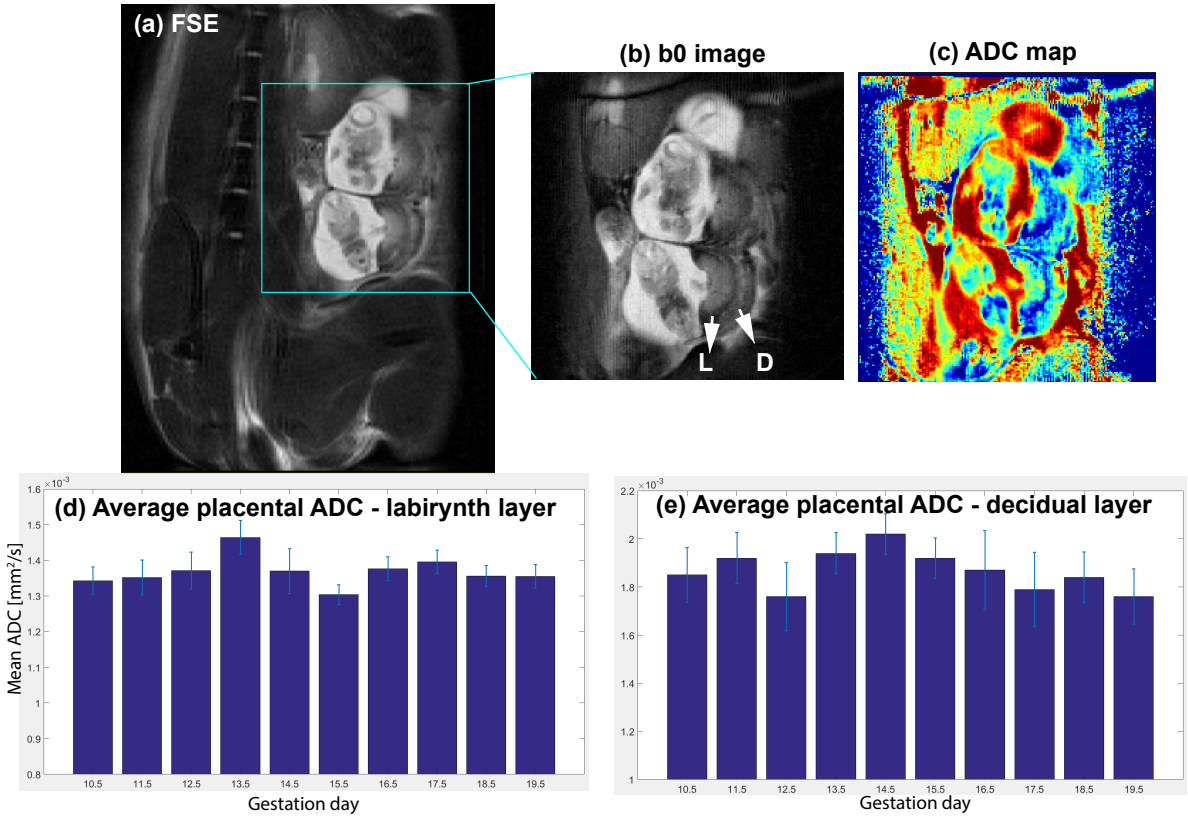

Figure 8. *In vivo* SPEN study of a mouse at E14.5. (a) FSE coronal slice, 55x40 mm in FOV and 1.5mm in thickness, illustrating two fetoplacental units. (b) b0 SPEN image zooming into the fetoplacental units with a 25x25 mm FOV (same slice thickness). (c) Corresponding ADC map collected with a 119 μm in-plane resolution. Arrows indicate the labyrinth (L) and decidual (D) layers in the placenta. Notice that these are separated by a layer of slowly diffusing water. (d,e) Systematic analyses of how average ADC values in the labyrinth and the decidual placental layers, change over time. Cohorts were as those leading to the data shown in Figure 7.

correction procedures that could successfully account for displacement-related artifacts between multiple interleaved shots. When operating in a zooming mode that is well suited to SPEN's reliance on swept pulses, the ensuing protocol provided the robustness needed to tackle in-plane resolutions on the order of 100μm –even if in the present case, sensitivity considerations limited the slice thicknesses that could be thus studied to larger (≈1mm) values. We are currently exploring whether alternative acquisition modes, including the use of cryogenically cooled surface coils, higher fields and denoising algorithms, could improve further the resolution of these experiments.

The new DWI scheme here introduced was used for an *in vivo* analysis of pregnant mice. Measurements revealed distinct diffusivity heterogeneities in the embryonic structures prior to

placentation; diffusivity differences within more mature fetoplacental units could also be observed, including components in fetal and newborn brains associated to CSF and to white matter, and a differentiation between the diffusivity of the decidual and chorionic layers within placentas. Diffusion characterizations of other, smaller structures including the fetal spine and the amniotic fluid, were also possible. Standard DWI techniques could also provide diffusivity maps for some of these structures for *ex vivo* fetoplacental units, yet these did not quantitatively recapitulate the *in vivo* measurements. An *in vivo* longitudinal follow-up also showed how the diffusivity within embryonic sacs changed with gestation, starting from the formation of gastrular heterogeneities, through the process of placentation, and onwards to the maturation of the fetal brain and spine.

From a biological standpoint, the features just summarized open a number of research questions worth exploring. One of these includes comparisons among various chemically and genetically induced disease models of pregnancy insufficiencies; preliminary results reveal significant differences between the diffusivity characteristics in those models vis-à-vis naïve mice[29]. Also worth evaluating is the potential usefulness of this kind of approaches, including the use of SPEN-customized parallel receive strategies[48], to the non-invasive *in utero* characterization of diffusion-based information in humans. From a methodological standpoint, it is likely that these measurements will benefit from parallel receiving advantages[49–51] that are of limited usefulness for the much smaller dimensions that characterize rodent research. Extensions that translate the phase corrections employed to correct SPEN-based interleaved acquisitions into descriptions of motions, are also worth exploring.

Acknowledgments. We are grateful to Mr. Koby Zibzener (Weizmann) for technical assistance, as well as to Drs. Zhiyong Zhang, Ricardo Martinho, Ron Hadas, Prof. M. Neeman (Weizmann) and Prof. M. Lustig (Weizmann/Berkeley) for valuable discussions. Financial support from the US NIH grant R01HD086323 (Human Placenta Project), the EU through ERC-2016-PoC grant # 751106, the Kimmel Institute for Magnetic Resonance and the generosity of the Perlman Family Foundation, are also acknowledged.

Author Contributions: QB, ES, GL & LF designed research; QB acquired the data; QB, ES, GL and LF contributed new tools and analyzed data; QB & LF wrote the paper.

Conflict of interests: The authors declare no competing financial interests.

References

1. Paul Callaghan. *Principles of nuclear magnetic resonance microscopy*. (Oxford, Clarendon Press; 1993).

2. Price, W. S. Pulsed-Field Gradient Nuclear Magnetic Resonance as a Tool for Studying Translational Diffusion: Part 1. Basic Theory. *Concepts Magn. Reson.* **9,** 299–336 (1997).

3. Price, W. S. Pulsed-field gradient nuclear magnetic resonance as a tool for studying translational diffusion: Part 2. Experimental aspects. *Concepts Magn. Reson.* **10,** 197–237 (1998).

4. Beaulieu, C. The basis of anisotropic water diffusion in the nervous system - A technical review. *NMR Biomed.* **15,** 435–455 (2002).

5. Le Bihan, D. The 'wet mind': Water and functional neuroimaging. *Phys. Med. Biol.* **52,** 57–89 (2007).

6. Le Bihan, D. Apparent diffusion Coefficient and Beyond: What Diffusion MR Imaging Can Tell Us about Tissue Structure. *Radiology* **268,** 318–322 (2013).

7. Basser, P. J., Mattiello, J., & LeBihan, D. MR diffusion tensor spectroscopy and imaging. *Biophys. J*, **66**, 259-267 (1994).

8. Stejskal, E. O. & Tanner, J. E. Spin diffusion measurements: Spin echoes in the presence of a time-dependent field gradient. *J. Chem. Phys.* **42,** 288–292 (1965).

9. Jones, D. K. *Diffusion MRI theory, methods, and applications*. (Oxford University Press, Oxford, 2011).

10. Mori S & Tournie J-D. *Introduction to Diffusion Tensor Imaging and Higher Order Models*. (Second Edition, Elsevier Ltd, Amsterdam, 2014).

11. Mansfield, P. Multi-planar image formation using NMR spin echoes. *J. Phys. C Solid State Phys.* **10,** L55–L58 (1977).

12. Schmitt K., Stehling R. & Turner, F. M. *Echo-Planar Imaging: Theory, Technique and Application*. (Springer Verlag, Heidelberg, 1998).

13. Stehling, M., Turner, R. & Mansfield, P. Echo-planar imaging: magnetic resonance imaging in a fraction of a second. *Science*. **254,** 43–50 (1991).

14. Rohde, G. K., Barnett, A. S., Basser, P. J., Marenco, S. & Pierpaoli, C. Comprehensive Approach for Correction of Motion and Distortion in Diffusion-Weighted MRI. *Magn. Reson. Med.* **51,** 103–114 (2004).

15. Mukherjee, P., Chung, S. W., Berman, J. I., Hess, C. P. & Henry, R. G. Diffusion tensor MR imaging and fiber tractography: Technical considerations. *Am. J. Neuroradiol.* **29,** 843–852 (2008).

16. Wu, W. & Miller, K. L. Image formation in diffusion MRI: A review of recent technical developments. *J. Magn. Reson. Imaging* **46,** 646–662 (2017).

17. Wang, F. N. *et al*. PROPELLER EPI: An MRI technique suitable for diffusion tensor imaging at high field strength with reduced geometric distortions. *Magn. Reson. Med.* **54,** 1232–1240 (2005).

18. Bammer, R., Holdsworth, S. J., Veldhuis, W. B. & Skare, S. T. New Methods in

Diffusion-Weighted and Diffusion Tensor Imaging. *Magn. Reson. Imaging Clin. N. Am.* **17,** 175–204 (2009).

19. Porter, D. A. & Heidemann, R. M. High resolution diffusion-weighted imaging using readout-segmented echo-planar imaging, parallel imaging and a two-dimensional navigator-based reacquisition. *Magn. Reson. Med.* **62,** 468–475 (2009).

20. Aggarwal, M., Mori, S., Shimogori, T., Blackshaw, S. & Zhang, J. Three-dimensional diffusion tensor microimaging for anatomical characterization of the mouse brain. *Magn. Reson. Med.* **64,** 249–261 (2010).

21. Wu, D., Lei, J., Rosenzweig, J. M., Burd, I. & Zhang, J. In utero localized diffusion MRI of the embryonic mouse brain microstructure and injury. *J. Magn. Reson. Imaging* **42,** 717–728 (2015).

22. Wu, D. & Zhang, J. In vivo mapping of macroscopic neuronal projections in the mouse hippocampus using high-resolution diffusion MRI. *Neuroimage* **125,** 84–93 (2016).

23. Wu, D. & Zhang, J. Recent Progress in Magnetic Resonance Imaging of the Embryonic and Neonatal Mouse Brain. *Front. Neuroanat.* **10,** 1–8 (2016).

24. Taviani, V. *et al.* High-resolution diffusion-weighted imaging of the breast with multiband 2D radiofrequency pulses and a generalized parallel imaging reconstruction. *Magn. Reson. Med.* **77,** 209–220 (2017).

25. Tal, A. & Frydman, L. Single-scan multidimensional magnetic resonance. *Prog. Nucl. Magn. Reson. Spectrosc.* **57,** 241–292 (2010).

26. Ben-Eliezer, N. & Frydman, L. Spatiotemporal encoding as a robust basis for fast three-dimensional in vivo MRI. *NMR Biomed.* **24,** 1191–1201 (2011).

27. Solomon, E. *et al.* Major mouse placental compartments revealed by diffusion-weighted MRI, contrast-enhanced MRI, and fluorescence imaging. *Proc. Natl. Acad. Sci.* **111,** 10353–10358 (2014).

28. Bao, Q., Liberman, G., Solomon, E., Lustig, M. & Fydman, L. Diffusion-weighted in vivo imaging with ≤100 μm resolution: Principles and applications to ADC mapping of pregnant mice. *Proc. Intl. Soc. Mag. Res. Med.* 1021 (2018).

29. Bao, Q. *et al.* High resolution diffusion MRI maps of mice with normal and dysfunctional placentas reveal clear fetal differences. *Proc. Intl. Soc. Mag. Res. Med.* 1035 (2018).

30. Solomon, E., Liberman, G., Nissan, N. & Frydman, L. Robust diffusion tensor imaging by spatiotemporal encoding: Principles and in vivo demonstrations. *Magn. Reson. Med.* **77,** 1124–1133 (2017).

31. Solomon, E. *et al.* Overcoming limitations in diffusion-weighted MRI of breast by spatio-temporal encoding. *Magn. Reson. Med.* **73,** 2163–2173 (2015).

32. Butts, K., Riederer, S. J., Ehman, R. L., Thompson, R. M. & Jack, C. R. Interleaved echo planar imaging on a standard MRI system. *Magn. Reson. Med.* **31,** 67–72 (1994).

33. Gu, H. *et al.* Single-shot interleaved z-shim EPI with optimized compensation for signal losses due to susceptibility-induced field inhomogeneity at 3 T. *Neuroimage* **17,** 1358–1364 (2002).

34. Seginer, A., Schmidt, R., Leftin, A., Solomon, E. & Frydman, L. Referenceless reconstruction of spatiotemporally encoded imaging data: Principles and applications to real-time MRI. *Magn. Reson. Med.* **72,** 1687–1695 (2014).

35. Schmidt, R., Seginer, A. & Frydman, L. Interleaved multishot imaging by spatiotemporal encoding: A fast, self-referenced method for high-definition diffusion and functional MRI. *Magn. Reson. Med.* **75,** 1935–1948 (2016).

36. Yang, Q. X., Posse, S., Bihan, D. L. E. & Smith, M. B. Double-sampled echo-planar imaging at 3 tesla. *J. Magn. Reson. - Ser. B* **113,** 145–150 (1996).

37. Andersson, J. L. R., Skare, S. & Ashburner, J. How to correct susceptibility distortions in spin-echo echo-planar images: Application to diffusion tensor imaging. *Neuroimage* **20,** 870–888 (2003).

38. Embleton, K. V., Haroon, H. A., Morris, D. M., Ralph, M. A. L. & Parker, G. J. M. Distortion correction for diffusion-weighted MRI tractography and fMRI in the temporal lobes. *Hum. Brain Mapp.* **31,** 1570–1587 (2010).

39. In, M. H., Posnansky, O., Beall, E. B., Lowe, M. J. & Speck, O. Distortion correction in EPI using an extended PSF method with a reversed phase gradient approach. *PLoS One* **10,** 1–19 (2015).

40. Solomon, E., Shemesh, N. & Frydman, L. Diffusion weighted MRI by spatiotemporal encoding: Analytical description and in vivo validations. *J. Magn. Reson.* **232,** 76–86 (2013).

41. Rivera-Pérez, J. A. & Hadjantonakis, A. K. The dynamics of morphogenesis in the early mouse embryo. *Cold Spring Harb. Perspect. Biol.* **7,** a015867 (2015).

42. Schneider, J. F. *et al.* Diffusion-weighted imaging in normal fetal brain maturation. *Eur. Radiol.* **17,** 2422–2429 (2007).

43. Rau, P. R. *et al.* Apparent diffusion coefficient in the aging mouse brain: A magnetic resonance imaging study. *Life Sci.* **78,** 1175–1180 (2006).

44. Renfree, M. B., Hensleigh, H. C. & McLaren, A. Developmental changes in the composition and amount of mouse fetal fluids. *J Embryol Exp Morphol* **33,** 435–446 (1975).

45. Cheung, C. Y. & Brace, R. A. Amniotic fluid volume and composition in mouse pregnancy. *J. Soc. Gynecol. Investig.* **12,** 558–562 (2005).

46. Capuani, S. *et al.* Diffusion and perfusion quantified by Magnetic Resonance Imaging are markers of human placenta development in normal pregnancy. *Placenta* **58,** 33–39 (2017).

47. Yadav, B. K. *et al.* A longitudinal study of placental perfusion using dynamic contrast enhanced magnetic resonance imaging in murine pregnancy. *Placenta* **43,** 90–97 (2016).

48. Liberman, G., Solomon, E., Lustig, M. & Frydman, L. Multiple-coil k-space interpolation enhances resolution in single-shot spatiotemporal MRI. *Magn. Reson. Med.* **79,** 796–805 (2018).

49. Guhaniyogi, S., Chu, M. L., Chang, H. C., Song, A. W. & Chen, N. K. Motion immune diffusion imaging using augmented MUSE for high-resolution multi-shot EPI. *Magn. Reson. Med.* **75,** 639–652 (2016).

50. Griswold, M. A. *et al.* Generalized Autocalibrating Partially Parallel Acquisitions (GRAPPA). *Magn. Reson. Med.* **47,** 1202–1210 (2002).

51. Barth, M., Breuer, F., Koopmans, P. J., Norris, D. G. & Poser, B. A. Simultaneous multislice (SMS) imaging techniques. *Magn. Reson. Med.* **75,** 63–81 (2016).